Volume 3 | Number 47 | 21 December 2015 | Pages 23623–24170

Journal of Materials Chemistry A

Materials for energy and sustainability

www.rsc.org/MaterialsA

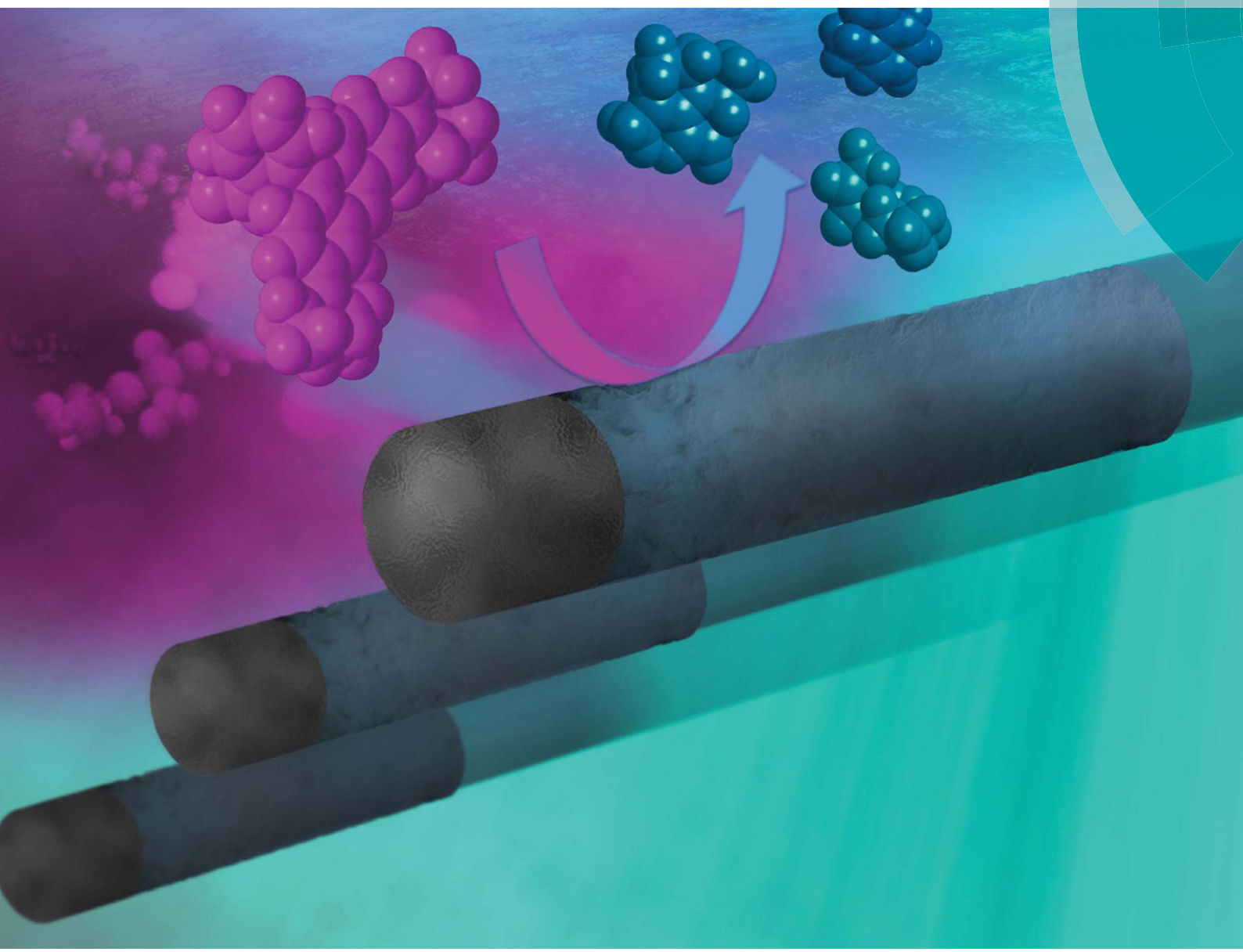

ISSN 2050-7488

ROYAL SOCIETY OF CHEMISTRY

PAPER

Miguel Guerrero, Salvador Pané *et al.*

Magnetically driven Bi_2O_3/BiOCl-based hybrid microrobots for photocatalytic water remediation

Journal of Materials Chemistry A

PAPER

View Article Online
View Journal | View Issue

Cite this: J. Mater. Chem. A, 2015, 3, 23670

Magnetically driven Bi_2O_3/BiOCl-based hybrid microrobots for photocatalytic water remediation†

Fajer Mushtaq,‡[a] Miguel Guerrero,‡*[b] Mahmut Selman Sakar,[a] Marcus Hoop,[a] André M. Lindo,[ac] Jordi Sort,[d] Xiangzhong Chen,[a] Bradley J. Nelson,[a] Eva Pellicer[b] and Salvador Pané*[a]

Received 28th July 2015
Accepted 28th September 2015

DOI: 10.1039/c5ta05825b

www.rsc.org/MaterialsA

In this work, we have developed 3D hybrid microstructures consisting of a short ferromagnetic CoNi segment for wireless magnetic control, coupled to a photocatalytic Bi_2O_3/BiOCl segment for water remediation under UV-visible light. These hybrid microstructures (pillars and helices) were fabricated using 3D photolithography and template-assisted electrodeposition, followed by *in situ* creation of a Bi_2O_3/BiOCl heterojunction after oxidation of Bi. This heterojunction is not only active under a wider solar spectrum but also ensures sufficient charge separation and hence low electron–hole recombination rate. As a result, these hybrid microstructures were able to degrade rhodamine B dye with a 90% efficiency in 6 hours. On application of magnetic fields we were able to precisely control the structures and collect them for reuse. Cytotoxicity tests were performed on our hybrid structures and a 95% cell viability was reported showing that our structures are biocompatible.

Introduction

Rapid industrialization, population growth and long periods of drought are imposing an increasing demand on clean water sources worldwide. It is estimated that 4 billion people have little to no access to clean water and millions of people die from waterborne diseases each year.[1] Thus, it is of utmost importance to develop low-cost, green, and highly efficient water treatment techniques.[2,3] Currently available water cleaning techniques such as adsorption and coagulation merely concentrate and transfer the pollutants to other phases without actually degrading them.[4–6] Other conventional water purification techniques include sedimentation and filtration, both of which, apart from being very expensive, also generate toxic secondary pollutants back into the environment.[7] Chlorination is one of the most widely practiced water disinfection processes, but it generates mutagenic and carcinogenic by-products that are harmful to human health.[1,8] These are the reasons why the field of "Advanced Oxidation Processes" (AOPs) for water purification is of intense current interest.[9] AOPs are based on the *in situ* generation of highly reactive transitory species such as hydroxyl and superoxide anion radicals ($OH^{\bullet}$ and $O_2^{\bullet-}$, respectively) for the degradation of organic compounds, pathogens and disinfection by-products.[9–12] Among these AOPs, heterogeneous photocatalysis has proven to be a cheap, efficient and green water remediation technique that works under ambient temperature and pressure and completely degrades the pollutants into harmless products like CO_2 and H_2O.[12–15]

Heterogeneous photocatalytic materials based on TiO_2 have attracted significant research in recent years since they have a high quantum yield due to their large band-gap.[7,16] These wide band-gap materials are popular, because they provide sufficient charge separation between the photogenerated electron–hole pairs. However, they have a major disadvantage of only being functional under UV light, which accounts for just 5% of the total solar spectrum. Hence, additional solutions such as doping or creating complex heterojunctions between different semiconductors having unequal band gaps are needed to make use of these materials under visible light.[16–18] To circumvent these challenges and to utilize solar energy more efficiently, a great deal of effort has been made to develop materials that can harvest a wide spectrum of visible light.[19] Visible-light induced photocatalysts are one of these materials, since visible light accounts for 48% of the total solar spectrum.[20] In this area, bismuth oxide (Bi_2O_3) is a promising visible light photocatalyst with a band gap of 2.8 eV. It also possesses unique optical and electrical properties, is biocompatible, and is capable of being fabricated by electrochemical means.[21] However, using Bi_2O_3

[a]Institute of Robotics and Intelligent Systems (IRIS), ETH Zurich, CH-8092 Zurich, Switzerland. E-mail: vidalp@ethz.ch

[b]Departament de Física, Facultat de Ciències, Universitat Autònoma de Barcelona, Campus UAB, E-08193 Bellaterra, Spain. E-mail: miguel.guerrero@uab.cat

[c]Instituto de Ciências Biomédicas Abel Salazar da Universidade do Porto, 4099-003 Porto, Portugal

[d]Institució Catalana de Recerca i Estudis Avançats (ICREA) and Departament de Física, Universitat Autònoma de Barcelona, E-08193 Bellaterra, Spain

† Electronic supplementary information (ESI) available: Fabrication versatility, EDX map of the as-prepared micropillars, photocatalytic degradation plots, biocompatibility characterization and videos of magnetic manipulation. See DOI: 10.1039/c5ta05825b

‡ Authors contributed equally to this work.

for practical applications is challenging due to its rapid recombination of photogenerated electron–hole pairs leading to a low quantum yield.[22] In contrast, bismuth oxychloride (BiOCl) is a highly efficient photocatalyst due to its wide band-gap of 3.6 eV, but this also makes its use limited to UV light.[20,23–25] Hence, by coupling Bi_2O_3 with BiOCl, sufficient separation between photogenerated electron–hole pairs can be created by charge transfer, resulting in enhancement of photocatalytic performance.[26,27] This heterojunction-based photocatalyst can be used under both UV and visible light sources and hence, can utilize a wider solar spectrum. Another advantage of using a bismuth oxide based photocatalyst is the *in situ* creation of a Bi_2O_3/BiOCl heterojunction which does not require any extra intermediate fabrication steps, making it a cheap and feasible technique.

Apart from the appropriate material selection, the size, shape and morphology of the photocatalyst also play a vital role in its efficiency. Due to their small size, the use of nanoparticles and nanofibers for water remediation usually results in either their coagulation, leading to a decreased active surface area, or in their loss which causes further pollution.[28] This makes such nanostructures an expensive and inefficient way to purify water. For a cost-effective and efficient way to clean water, it is thus necessary to design structures that can be easily recovered for their subsequent reuse. Moreover, altering the morphology of the photocatalyst by inducing porosity leads to a substantial enhancement in its photocatalytic activity due to an increased surface area.

At present, research is being carried out for developing new environmental micro- and nanorobots that can kill pathogens, degrade organic pollutants, and remove heavy metals and oil from water.[29] The use of nanoparticles for water remediation has been extensively explored in the last few years but presents many limitations as discussed earlier.[30] Catalytically powered micro- and nanomotors that rely on hydrogen peroxide for propulsion have also attracted considerable attention for cleaning water. The use of electromagnetic fields, on the other hand, offers an efficient and environmentally friendly technique to wirelessly power micro and nanomotors.[30–32]

Experimental

Fabrication of 3D microcavities

Commercially available circular microscopic glass slides with a diameter of 30 mm were used as substrates. A 25 nm thick ITO layer was evaporated on the glass slides using a UNIVEX 500 e-beam evaporator. A rapid thermal annealing oven (JetFirst100) was used to anneal the ITO layer at 550 °C for 5 minutes to render the slides transparent for 3D laser lithography. A 20 μm thick positive-tone photoresist AZ 9260 (MicroChemicals) was spin-coated on the substrate and used for the direct laser writing (DLW) process to create three dimensional (3D) microgeometries of pillars and helices in the resist (Nanoscribe GmbH, Germany) at a speed of 3500 structures per h. The laser exposed samples were then developed for 30 min in a AZ 400K developer (MicroChemicals) at a 1 : 4 ratio in DI water.

Electrodeposition of the cobalt-nickel (CoNi) segment

Prior to electrodeposition the microcavities were placed in a vacuum pump under low pressure for 10 min with a drop of DI water covering them to remove any trapped air bubbles. CoNi was deposited at the bottom of the microcavities by using the following electrolyte composition: 300 g L^{-1} $NiSO_4 \cdot 6H_2O$, 30 g L^{-1} $NiCl_2 \cdot 6H_2O$, 40 g L^{-1} $CoSO_4 \cdot 6H_2O$, 40 g L^{-1} $C_6H_8O_7$, 20 g L^{-1} H_3BO_3, 2 g L^{-1} $C_7H_5NO_3S$, and 3 mL L^{-1} tergitol 08. The pulse electrodeposition (PED) technique was used to deposit CoNi in the cavities using a potentiostat (Autolab PGSTAT302N) at a current density of 50 mA cm^{-2} with a cathodic pulse length of 4 ms and a rest pulse of 10 ms. The deposition was carried out in a chemical cell at 55 °C with a magnetic stirring rate of 400 rpm. A nickel sheet was used as the counter electrode. Deposition was carried out to obtain a 2 μm long CoNi segment for micropillars and 0.5 μm for microhelices.

Electrodeposition of the Bi/BiOCl segment

To deposit Bi/BiOCl on top of the CoNi segment a chemical bath with the following composition was used: 2.53 g L^{-1} $BiCl_3$, 2.34 g L^{-1} NaCl, 1.2 M HCl and 0.23 mL L^{-1} Triton X-100. A PED technique was also used to deposit the photocatalytic segment at a current density of 25 mA cm^{-2} with a cathodic pulse length of 4 ms and a rest pulse of 10 ms using the same potentiostat. The deposition was carried out in a chemical cell at room temperature with a magnetic stirring rate of 400 rpm. A platinum sheet was used as the counter electrode. Electrodeposition was performed until a 10 μm long Bi/BiOCl segment was deposited. After electrodeposition, free-standing microstructures were obtained by dissolving the photoresist in acetone, isopropanol and DI water. These free-standing structures were immersed in DI water under UV light for 6 hours to convert Bi to Bi_2O_3.

Structural characterization

Scanning electron microscopy (SEM) characterization was performed using a Zeiss ULTRA 55 at 2 kV with an SE2 and InLens detector. A Zeiss NVision 40 was used to perform energy dispersive X-ray (EDX) measurements and to do focused ion beam (FIB) cuts on the cross-section of free-standing microstructures. A Bruker AXS D8 Advance equipped with a Lynxeye superspeed detector and a Cu K(α) radiation source was used at room temperature to perform X-ray diffraction (XRD) measurements. Transmission electron microscopy (TEM) analyses were done on a Jeol-JEM 2011 microscope operating at 200 kV. UV-vis diffuse reflectance spectra (DRS) were acquired by using a Cary 4000 UV-vis spectrophotometer. $BaSO_4$ was used as the reflectance standard.

Photocatalytic characterization

Photocatalytic experiments were performed to study the degradation of Rhodamine-B (RhB) dye over time. For this, a calibration curve for RhB solution was obtained to study the concentrations at which RhB has a linear curve (Fig. S4a†). A RhB concentration of 50 μg L^{-1} was chosen to perform

degradation experiments. A free-standing array of hybrid microstructures (12 mg L^{-1}) on an ITO slide was placed in a 10 mL solution of RhB and irradiated with UV-visible light (320–500 nm) using a 400 W tungsten lamp. A UV-vis spectrophotometer (Tecan Infinite 200 Pro) was used to obtain the fluorescence spectra of RhB over time by taking aliquots of irradiated RhB solution at 0, 30, 60, 120, 240 and 360 min (Fig. S4b†).

Biocompatibility test

NIH 3T3 cells (American Type Cell Culture, ATCC) were expanded in high glucose (4.5 g L^{-1}) DMEM containing (GIBCO), 10% bovine serum and 100 units per mL penicillin and 100 mg mL^{-1} streptomycin. The cells were labeled with Hoechst 33342 (Sigma) and Alexa 488 Phalloidin (Sigma). Phase-contrast and fluorescence images were taken (Fig. S5a†) with an IX81 Olympus camera at 10× magnification. The MTT cytotoxicity study was conducted in a flat bottomed 24-well plate with 1×10^5 3T3 cells in 1 mL culture medium per well. Cells were allowed to attach on the substrate with free-standing CoNi–Bi_2O_3/BiOCl pillars overnight. Then, the cell culture medium was supplemented with 100 μL of 12 mM MTT. Cells were further incubated for 4 h for MTT cleavage at 37 °C. Then, 100 μL of isopropanol and 0.04 M HCl were added to each well and mixed thoroughly until the formazan crystals were dissolved. Absorbance measurements were conducted in a microtiter plate reader (Infinite F200 Tecan) at 570 nm. Reported values (Fig. S5b†) are represented as mean values of three independent replicates as percentages with respect to the control sample.

Magnetic manipulation

Free-standing hybrid CoNi–Bi_2O_3/BiOCl microstructures were released in DI water using gentle sonication for 30 min. The magnetic manipulation system consists of eight stationary electromagnets with soft magnetic cores and is capable of producing magnetic fields and gradients up to 50 mT and 0.5 T m^{-1} at frequencies up to 100 Hz.[34] The system is integrated with an inverted fluorescence microscope (Olympus IX 81) and videos of manipulated structures were recorded at 50× magnification as can been seen in Videos S1 and S2.†

Results and discussion

In this work, we report the fabrication of novel, photocatalytic micromachines that degrade the organic pollutant RhB under UV-visible light and can be magnetically manipulated. These microstructures consist of a ferromagnetic CoNi segment, which allows them to be guided using external magnetic fields. On the magnetic segment a porous, photoactive Bi_2O_3/BiOCl segment is grown. The photocatalytic performance of these microstructures was evaluated by measuring the decrease of RhB dye to demonstrate 90% dye removal efficiency. These hybrid microrobots were precisely controlled wirelessly using external magnetic fields and showed no cytotoxic effects towards cells, hence indicating their possible use for cleaning water with aquatic life. Hybrid micropillars and microhelices were fabricated using template-assisted electrodeposition. 3D photolithography provides the opportunity to batch fabricate free-standing microcavities with various dimensions and shapes (Fig. S1a–c†) in a regular array. In our work, microcavities with a diameter of 1.5 μm were created inside a 20 μm thick photoresist layer using DLW. These microcavities were then filled by sequential electrodeposition using two different electrolytes. In Fig. 1a we can see the scheme followed to fabricate these microstructures where microcavities were formed inside a photoresist layer. A short CoNi segment was then electrochemically deposited at the bottom of the microcavity by using PED. Its length was optimized by controlling the electrodeposition time to obtain a surface-walker motion for micropillars and a corkscrew motion for microhelices. Consequently, the deposition of a longer Bi/BiOCl segment was followed by PED for depositing the photocatalytic segment. The use of PED leads to the formation of porous Bi/BiOCl segments. To reveal free-standing microstructures as presented in the SEM image in Fig. 1b, the photoresist layer was dissolved by immersing the substrate in acetone, isopropanol and DI water. Fig. 1c and d show SEM images displaying hybrid micropillars and microhelices. In both these images we can observe a short and compact CoNi segment followed by a longer, porous Bi/BiOCl segment, which can in turn enhance the diffusion of reactants/products and increase the photocatalytic activity of the hybrid structures. The SEM image in Fig. 1e shows a FIB cut performed on a free-standing hybrid micropillar. A robust and smooth interface between the CoNi and Bi/BiOCl segments is revealed which is necessary to keep the two segments intact during motion in complex environments.

Elemental analysis was performed on the as-prepared hybrid micropillars by EDX. This analysis confirmed that the ferromagnetic segment is composed of 52% Co and 48% Ni. The photocatalytic segment showed a strong presence of Bi and a relatively weak signal for O and Cl which could predominantly arise from the presence of BiOCl (Fig. S2a†). The crystalline structure of the hybrid samples was analyzed using XRD on an array of free-standing micropillars before and after exposure to water under UV light (Fig. 2a). The XRD pattern shows a strong presence of metallic Bi and BiOCl and very small Bi_2O_3 peaks. Complementary TEM analyses are shown in the ESI† for the as-prepared micropillars (Fig. S3†). In order to create the Bi_2O_3/BiOCl heterojunction, Bi was oxidized to Bi_2O_3 by exposing the as-prepared hybrid microstructures to a UV light source in water for 6 hours. After exposure to water, there is no detectable change in the BiOCl phase structure (JCPDS file no. 06-0249) as shown in the diffraction peaks (Fig. 2a). However, some new diffraction peaks at 27.5°, 31.8°, 45.6°, 56.6°, 66.3°, 75.4° and 84.1° can be observed corresponding to the (111), (200), (220), (222), (400), (420) and (422) crystal planes of δ-Bi_2O_3 (JCPDS file no. 77-0374) while the intensity of (104) and (122) reflections at 38.3° and 64.6° observed for metallic Bi (JCPDS file no. 44-1246) have decreased. This indicates that metallic Bi is oxidized to the Bi_2O_3 phase during exposure to water under UV light.[26] The results of EDX analysis performed on the exposed hybrid

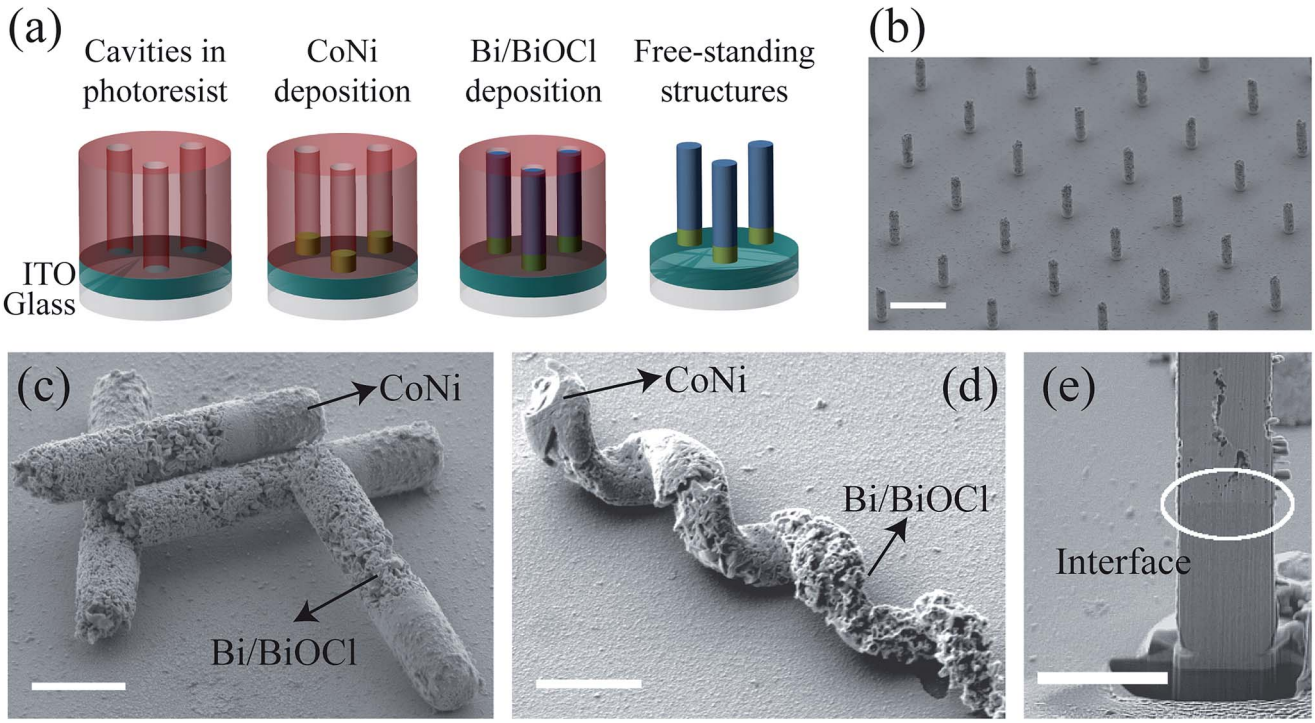

Fig. 1 Fabrication of hybrid microstructures. (a) Schematic showing microcavities formed inside a positive photoresist, spin coated onto an ITO covered glass slide, followed by electrodeposition of CoNi and Bi/BiOCl segments to form free-standing structures by dissolving the resist; (b) array of free-standing hybrid micropillars; (c) hybrid micropillars and (d) hybrid microhelices; (e) SEM image produced by performing a FIB cut on a hybrid micropillar. Scale bars indicate 10 μm (b), 2 μm (c–e).

structures are in agreement with these XRD results where the ferromagnetic segment's composition remained unchanged, but the photocatalytic segment showed a very strong oxygen signal and a relatively weak Bi signal. This again points towards the *in situ* oxidation of Bi to Bi_2O_3 after water exposure. Fig. 2b shows the EDX mapping obtained for the exposed hybrid micropillars, where the ferromagnetic segment has a homogeneous Co and Ni distribution, and, similarly, the photocatalytic segment depicts a uniform distribution of Bi, O and Cl. Comparison between this EDX mapping and the EDX mapping corresponding to the as-prepared hybrid micropillar (Fig. S2a†) reveals that after exposure the intensity of Bi is reduced while that of O increased. From these results we can conclude that metallic Bi oxidizes to Bi_2O_3. Furthermore, UV-vis DRS was performed to determine the optical properties of the samples (Fig. S2d†). The as-prepared samples showed a stronger absorption in the 200–370 nm spectrum while after UV-light exposure, the samples showed absorbance in the range of 200–450 nm. These results again indicate the presence of visible light active Bi_2O_3 coupled to UV-light active BiOCl.

Photocatalytic performance of the hybrid micropillars was evaluated by degradation of RhB solution under UV-visible light for 6 hours after the adsorption–desorption equilibrium was reached. The degradation curve in Fig. 3a presents 90% dye removal efficiency in the presence of hybrid micropillars. Notice that 6 h is not an exceedingly long time considering the relatively low catalyst amount (12 mg L^{-1}) and high dye concentration (50 mg L^{-1}). For example, degradation of 86% of the initial RhB concentration (10 mg L^{-1}) was accomplished using 300 mg L^{-1} of BiOCl/TiO_2 composite catalyst under UV-vis light irradiation in 3 h.[23] In our case the catalyst amount is 25 times lower and the dye concentration is 5 times higher, therefore the degradation rate is indeed rather high. Additional experiments were also performed to ensure that light irradiation had little effect on RhB concentration in the presence of the control sample and the substrate. From the degradation curve it can be seen that in the absence of the hybrid sample, a dye degradation of more than 10% could not be achieved even after 6 hours. This photocatalytic degradation study in the presence of hybrid micropillars was performed on six different samples to ensure a good reproducibility, which can also be observed from the small standard deviation values seen in the curve. The reusability of hybrid micropillars was tested for the same sample under identical reaction conditions for three consecutive cycles. It was found that after the first run the degradation rate slightly increased which is evident from a steeper slope obtained for runs two and three (Fig. 3b). This lower dye degradation rate during the first run can be explained by the still on-going *in situ* oxidation of Bi to Bi_2O_3 when exposed to water. Degradation curves for runs two and three showed an identical, enhanced behavior, hence demonstrating that these hybrid microstructures can be efficiently reused for multiple dye degradation studies. Kinetics of the RhB degradation reaction for cycle 1 and cycle 3, presented in Fig. 3c, follows a pseudo-first-order reaction given by the eqn (1):

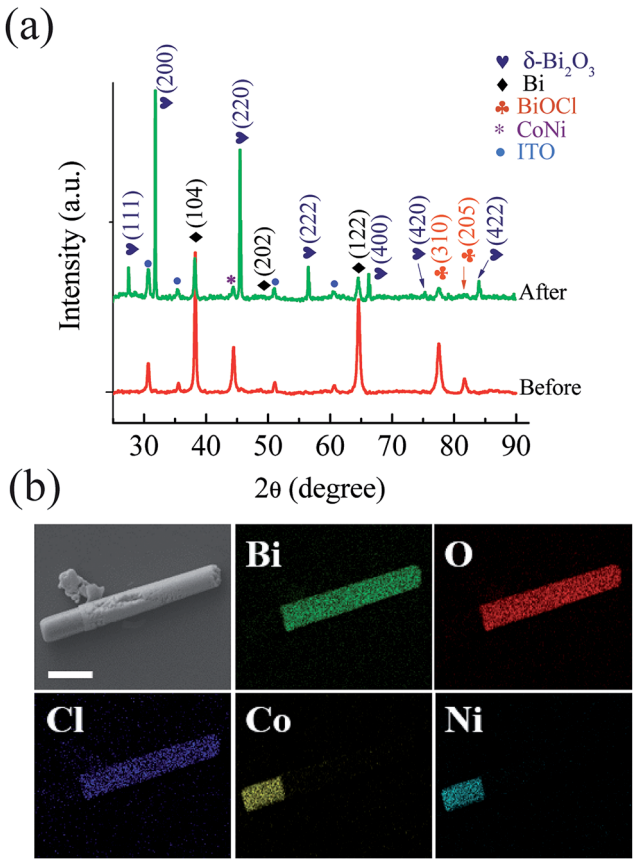

Fig. 2 Structural characterization of hybrid micropillars. (a) XRD patterns of hybrid micropillars before and after exposure to water under UV light for 6 hours; (b) EDX mapping showing distribution of elements in an exposed hybrid micropillar (scale bar 2 μm).

$$\ln\frac{C_0}{C} = kt \quad (1)$$

where k is the reaction rate constant, C_0 is the initial RhB concentration, and C is the RhB concentration at time t. The slope of the degradation plot obtained for the first run gives a k value of 0.0075 min^{-1}, which is in good agreement with the literature.[12,18,22] For the third run, after the *in situ* oxidation of Bi to Bi_2O_3, a higher k value of 0.0096 min^{-1} was calculated. This quantitatively describes the enhanced performance of the hybrid structures after their first run.

Photocatalytic degradation of organic pollutants is attributed to the formation of electron–hole pairs on the surface of semiconductors upon light illumination. The proposed photocatalytic degradation scheme for hybrid micropillars is illustrated in Fig. 3d. From this figure we can see that BiOCl and Bi_2O_3 promote photocatalytic degradation under UV and visible light, due to their band gaps of 3.6 eV and 2.8 eV, respectively. The heterojunction between BiOCl and Bi_2O_3 is reported to demonstrate 10–15 times higher photocatalytic activity under UV-visible light due to the unique relative band position of these two semiconductors.[27,28] Due to a relatively smaller band gap the electrons in the valence band (VB) of Bi_2O_3 are excited to its conduction band (CB) upon irradiation of visible light. These

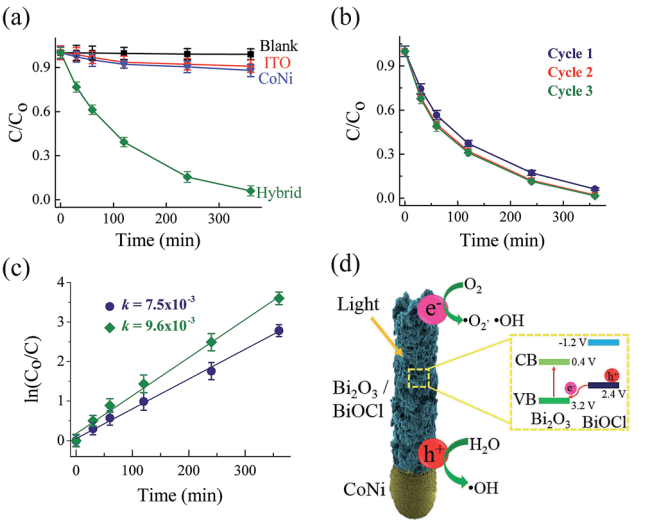

Fig. 3 Photocatalytic degradation of hybrid micropillars. (a) Photocatalytic degradation curves of blank, ITO covered glass slide, free-standing CoNi, and hybrid structures upon light irradiation; (b) plot showing degradation curve results for three consecutive runs for the same sample; (c) linear fit log plot of the degradation curve for cycle 1 and 3 showing an enhanced k value for cycle 3; (d) photocatalytic degradation scheme of hybrid micropillars showing the formation of electron–hole pairs and how they degrade organic pollutants.

vacant sites in the VB of Bi_2O_3 are then occupied by the electrons in the VB of BiOCl, since the VB energy level of Bi_2O_3 is 0.8 eV lower than that of BiOCl. This initiates the formation of holes in the VB of BiOCl. Formation of a heterojunction between Bi_2O_3 and BiOCl thus separates the electron–hole pairs and prevents their recombination. These electron–hole pairs are responsible for initiating the photocatalytic reactions by converting oxygen and water to form highly reactive species such as $OH^{\bullet}$ and $O_2^{\bullet -}$. These radicals then are able to degrade organic pollutants into harmless products.[27,33]

In order to use these microstructures to clean water sources with aquatic life, it is important to ensure that they do not possess cytotoxic effects. Therefore, the interaction between the CoNi–Bi_2O_3/BiOCl micropillars and NIH 3T3 cells was examined. Cells were cultured on an array of free-standing hybrid micropillars for 48 hours. Fig. 4a shows an optical image of fibroblast cells cultured on a free-standing array of hybrid micropillars. From this image it can be seen that the cells adhered well on the substrate and extended protrusions over the surface of the pillars. These interactions led to the detachment of structures from the substrate. After 48 hours the substrates were covered with proliferating cells. The immunohistochemistry for F-actin showed apparently normal stress fibers. To further demonstrate this we performed nucleus and actin filament staining which showed viable cells growing over an array of hybrid structures (Fig. S5a†). Fig. 4b shows an SEM image of a healthy cell interacting with the hybrid structure. Altogether these results show that the microstructures are biocompatible. To ensure that these microstructures can be guided to specific locations and collected for re-use, the

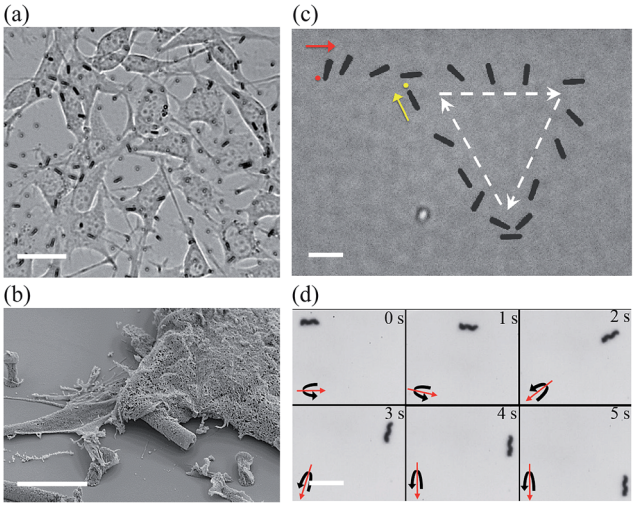

Fig. 4 Biocompatibility and magnetic manipulation of hybrid microstructures. (a) Optical image of cells cultured on an array of hybrid micropillars showing cell proliferation and detachment of structures; (b) SEM image showing the interaction between a micropillar and a cell; (c) magnetic manipulation of a hybrid micropillar showing a surface-walker motion; (d) magnetic manipulation of a hybrid microhelix demonstrating a corkscrew motion under rotational fields. Scale bars indicate 40 μm (a), 5 μm (b) and 10 μm (c and d).

micropillars and microhelices were tested for their magnetic response to wireless magnetic fields by releasing them from the substrate into a DI water solution. It was possible to precisely guide the magnetic microstructures along pre-planned trajectories (Fig. 4c and d, respectively). Under rotational magnetic fields the micropillars demonstrated a surface-walker motion on the substrate, whereas the microhelices were able to corkscrew in suspension making them useful in viscous environments and away from hard surfaces (Videos S1 and S2† respectively).[34] This ability to move microstructures with high precision and relatively low magnetic fields (less than 10 mT), allows them to be successfully collected and reused multiple times in complex microenvironments (Fig. S4c†). Apart from this, wireless control of hybrid microstructures also makes it possible to target polluted wastewater locations that are not easily accessible for conventional water treatment techniques.

Conclusion

In conclusion, we have developed novel hybrid micropillars and microhelices for water remediation under UV-visible light which consist of a ferromagnetic segment followed by a bismuth-based photocatalytic segment. These structures were fabricated using two subsequent electrodeposition procedures and in this work we have shown the possibility of patterning UV-visible light photocatalysts into different shapes. The as-fabricated photocatalytic part consists of a Bi/BiOCl porous segment which is oxidized to form a Bi_2O_3/BiOCl heterojunction photocatalyst. These microstructures were able to degrade the organic pollutant RhB *in situ* with 90% efficiency in 6 h under a UV-visible light source. Photocatalytic degradation studies conducted on these structures demonstrated good repeatability and reusability. These biocompatible microstructures were precisely controlled and guided using external magnetic fields allowing them to be collected and reused for further degradation experiments, hence making them an economic and efficient material to clean natural water sources.

Acknowledgements

This work has been partially financed by the European Research Council Starting Grant "Magnetoelectric Chemonanorobotics for Chemical and Biomedical Applications (ELECTROCHEMBOTS)", by the ERC grant agreement no. 336456. Dr Miguel Guerrero acknowledges the Swiss National Science Foundation for the grant "Individual short research visits" (IZK0Z2_150931), and the support of the Secretary for Universities and Research of the Government of Catalonia and the COFUND Programme of the Marie Curie Actions of the 7th R&D Framework Programme of the European Union for the '*Beatriu de Pinos*' contract (2013 BP-B 00077). Dr Eva Pellicer and Prof. Dr Jordi Sort acknowledge 2014-SGR-1015 project from the Generalitat de Catalunya, and the project MAT2014-57960-C3-1-R from the MICINN. Dr Eva Pellicer is also grateful to MINECO for the "Ramon y Cajal" contract (RYC-2012-10839). The authors would like to acknowledge the Scientific Center for Optical and Electron Microscopy (ScopeM) of ETH Zürich, Dr Davide Ferri from the Paul Scherrer Institute (PSI) for help with DRS measurements, and the FIRST laboratory for their technical support.

Notes and references

1 M. Pera-Titus, V. García-Molina, M. A. Baños, J. Giménez and S. Esplugas, *Appl. Catal., B*, 2004, **47**, 219.
2 N. Cheng, J. Tian, Q. Liu, C. Ge, A. H. Qusti, A. M. Asiri, A. O. Al-Youbi and X. Sun, *ACS Appl. Mater. Interfaces*, 2013, **5**, 6815.
3 V. I. Parvulescu and H. Garcia, *Faraday Discuss. R. Soc. Chem.*, 2011, **23**, 204.
4 X. Qu, P. J. J. Alvarez and Q. Li, *Air, Soil Water Res.*, 2013, **47**, 3931.
5 D. Mohan and C. U. Pittman Jr, *J. Hazard. Mater.*, 2007, **142**, 1.
6 A. Matilainen, M. Vepsäläinen and M. Sillanpää, *Adv. Colloid Interface Sci.*, 2010, **159**, 189.
7 M. N. Chong, B. Jin, C. W. K. Chow and C. Saint, *Air, Soil Water Res.*, 2010, **44**, 2997.
8 J. Lu, T. Zhang, J. Ma and Z. Chen, *Hazard. Mater.*, 2009, **162**, 140.
9 B. A. Wols and C. H. M. Hofman-Caris, *Air, Soil Water Res.*, 2012, **46**, 2815.
10 H. M. Coleman, C. P. Marquis, J. A. Scott, S. S. Chin and R. Amal, *Chem. Eng. J.*, 2005, **113**, 55.
11 U. Latif, J. Qian, S. Can and F. L. Dickert, *Sensors*, 2014, **14**, 23419.
12 Q. I. Rahman, M. Ahmad, S. K. Misra and M. Lohani, *Mater. Lett.*, 2013, **91**, 170.

13 S. Malato, P. Fernández-Ibáñez, M. I. Maldonado, J. Blanco and W. Gernjak, *Catal. Today*, 2009, **147**, 1.
14 U. I. Gaya and A. H. Abdullah, *J. Photochem. Photobiol., C*, 2008, **9**, 1.
15 S. Anandan, G.-J. Lee, P.-K. Chen, C. Fan and J. J. Wu, *Ind. Eng. Chem. Res.*, 2010, **49**, 9729.
16 Y. Yang and P. Wang, *Polymer*, 2006, **47**, 2683.
17 L. Zhang, J. Niu, D. Li, D. Gao and J. Shi, *Adv. Condens. Matter Phys.*, 2014, 6.
18 S. Balachandran and M. Swaminathan, *J. Phys. Chem. C*, 2012, **116**, 26306.
19 W. J. Youngblood, S.-H. A. Lee, K. Maeda and T. E. Mallouk, *Acc. Chem. Res.*, 2009, **42**, 1966.
20 J. Tian, Y. Sang, G. Yu, H. Jiang, X. Mu and H. Liu, *Adv. Mater.*, 2013, **25**, 5074.
21 Y. Gao, H. J. Xin, J. Shang, L. Wang, W. C. Hao and T. M. Wang, *Mater. Res. Innovations*, 2014, **18**, S4.
22 Q. Wang, J. Hui, L. Yang, H. Huang, Y. Cai, S. Yin and Y. Ding, *Appl. Surf. Sci.*, 2014, **289**, 224.
23 M. Guerrero, A. Altube, E. García-Lecina, E. Rossinyol, M. D. Baró, E. Pellicer and J. Sort, *ACS Appl. Mater. Interfaces*, 2014, **6**, 13994.
24 H.-Y. Jiang, J. Liu, K. Cheng, W. Sun and J. Lin, *J. Phys. Chem. C*, 2013, **117**, 20029.
25 X. Liu, L. Pan, T. Lv, Z. Sun and C. Q. Sun, *J. Colloid Interface Sci.*, 2013, **408**, 145.
26 J. Hu, G. Xu, J. Wang, J. Lv, X. Zhang, T. Xie, Z. Zheng and Y. Wu, *Dalton Trans.*, 2015, **44**, 5386.
27 S. Y. Chai, Y. J. Kim, M. H. Jung, A. K. Chakraborty, D. Jung and W. I. Lee, *J. Catal.*, 2009, **262**, 144.
28 C. Wang, C. Shao, Y. Liu and L. Zhang, *Scr. Mater.*, 2008, **59**, 332.
29 X. Ma, K. Hahn and S. Sanchez, *J. Am. Chem. Soc.*, 2015, **137**, 4976.
30 S. Sánchez, L. Soler and J. Katuri, *Angew. Chem., Int. Ed. Engl.*, 2015, **54**, 1414.
31 L. Soler and S. Sanchez, *Nanoscale*, 2014, **6**, 7175.
32 J. Wang and W. Gao, *ACS Nano*, 2012, **6**, 5745.
33 G. Li, B. Jiang, S. Xiao, Z. Lian, D. Zhang, J. C. Yu and H. Li, *Environ. Sci.: Processes Impacts*, 2014, **16**, 1975.
34 M. A. Zeeshan, R. Grisch, E. Pellicer, K. M. Sivaraman, K. E. Peyer, J. Sort, B. Özkale, M. S. Sakar, B. J. Nelson and S. Pané, *Small*, 2014, **10**, 1284.